


---

This is the **accepted version** of the journal article:

De Tovar Villanueva, Jonathan; Romero Fernández, Nuria; Denisov, Sergey A.; [et al.]. «Light-driven water oxidation using hybrid photosensitizer-decorated Co<sub>3</sub>O<sub>4</sub> nanoparticles». Materials Today Energy, Vol. 9 (September 2018), p. 506-515. DOI 10.1016/j.mtener.2018.07.008

---

This version is available at <https://ddd.uab.cat/record/289780>

under the terms of the  **CC BY** COPYRIGHT license

# Light-driven water oxidation using hybrid photosensitizer-decorated Co<sub>3</sub>O<sub>4</sub> nanoparticles

Jonathan De Tovar<sup>a</sup>, Nuria Romero<sup>a</sup>, Sergey Denisov<sup>b</sup>, Roger Bofill<sup>a</sup>, Carolina Gimbert-Suriñach<sup>c</sup>, Diana Ciuculescu-Pradines<sup>d</sup>, Samuel Drouet<sup>d</sup>, Antoni Llobet<sup>a,c</sup>, Pierre Lecante<sup>e</sup>, Vincent Colliere<sup>d</sup>, Zoraida Freixa<sup>f</sup>, Nathan McClenaghan<sup>b</sup>, Catherine Amiens<sup>d</sup>, Jordi García-Antón<sup>a,\*</sup>, Karine Philippot<sup>d,\*</sup>, and Xavier Sala<sup>a,\*</sup>

<sup>a</sup> Departament de Química, Facultat de Ciències  
Universitat Autònoma de Barcelona  
08193 Bellaterra, Catalonia (Spain)

<sup>b</sup> Institut des Sciences Moléculaires, Université Bordeaux / CNRS  
351 Cours de la Libération  
33405 Talence Cedex (France)

<sup>c</sup> Institut Català d'Investigació Química (ICIQ)  
Barcelona Institute of Science and Technology (BIST)  
Av. Països Catalans 16  
43007 Tarragona, Catalonia (Spain)

<sup>d</sup> LCC-CNRS, Université de Toulouse, CNRS, UPS  
205, route de Narbonne  
F-31077 Toulouse (France)  
E-mail:

<sup>e</sup> CNRS, CEMES (Centre d'Elaboration de Matériaux et d'Etudes Structurales)  
29 rue J. Marvig  
F-31055 Toulouse (France)

<sup>f</sup> Department of Applied Chemistry, Faculty of Chemistry  
University of the Basque Country (UPV-EHU)  
20080 San Sebastián (Spain) &  
IKERBASQUE, Basque Foundation for Science  
Bilbao (Spain)

\* Corresponding authors:

E-mail addresses: [Jordi.GarciaAnton@uab.es](mailto:Jordi.GarciaAnton@uab.es) (J. García-Antón), [Xavier.Sala@uab.cat](mailto:Xavier.Sala@uab.cat) (X. Sala), [Karine.Philippot@lcc-toulouse.fr](mailto:Karine.Philippot@lcc-toulouse.fr) (K. Philippot)

**Keywords:** Co<sub>3</sub>O<sub>4</sub> nanoparticles, water oxidation, dyad systems, electrocatalysis, photocatalysis

## ABSTRACT

Cobalt nanoparticles (NPs) have been prepared by hydrogenation of the organometallic complex  $[\text{Co}(\eta^3\text{-C}_8\text{H}_{13})(\eta^4\text{-C}_8\text{H}_{12})]$  in 1-heptanol in the absence of any other stabilizer and then transformed into  $\text{Co}_3\text{O}_4$  NPs using mild oxidative reaction conditions. After deposition onto glassy carbon rotating disk electrodes, the electrocatalytic performance of the  $\text{Co}_3\text{O}_4$  NPs in water oxidation has been tested in 1M NaOH. The activity has been benchmarked with that of state-of-the-art  $\text{Co}_3\text{O}_4$  NPs through electrochemically-active surface area (ECSA) and specific current density measurements. Furthermore, the covalent grafting of photosensitive polypyridyl-based  $\text{Ru}^{\text{II}}$  complexes onto the surface of  $\text{Co}_3\text{O}_4$  NPs afforded hybrid nanostructured materials able to photo-oxidize water into  $\text{O}_2$ , while steady-state and time-resolved spectroscopic measurements gave some further insight into kinetics and pertinent reaction steps following excitation. These first-row transition metal oxide hybrid nanocatalysts display better catalytic performance than simple mixtures of non-grafted photosensitizers and  $\text{Co}_3\text{O}_4$  NPs, thus evidencing the advantage of the direct coupling between the two entities for the photo-induced water oxidation reaction.

## 1. Introduction

Non-renewable fossil fuels are still nowadays the main energy source used by mankind. However, their fast depletion due to the constant increase of the global energy consumption and their relationship with worrying levels of greenhouse gases and climate change make the development of less polluting and renewable energy sources a central topic for the scientific community. In this context, the development of sunlight-driven water-splitting procedures is gaining momentum[1]. The water splitting reaction, in which both oxygen and hydrogen gas are generated in the anode and cathode, respectively, represents an attractive method for obtaining energy in the form of the highly energetic H–H chemical bond[2], as long as the energy used to produce the hydrogen gas is renewable. Nevertheless, the anodic oxidation of water into  $\text{O}_2$  is a thermodynamically uphill, mechanistically complex and kinetically slow process, in which four electrons have to be removed from two water molecules and an O=O double bond has to be formed[3]. With the aim of improving the kinetics of this half reaction and inspired by Nature's photosystem II, which is responsible for oxygen formation during photosynthesis, a range of photocatalytic systems has been developed during the past years[4,5]. Thus, several homogeneous and heterogeneous water oxidation catalysts (WOCs) have been tested in the presence of a photosensitizer (PS), a chromophore able to harvest photons and harness their energy to transfer electrons[6]. However, the catalytic performance of these systems is often limited by the insufficient rate of electron transfer from the WOC to the PS and the undesired back-electron transfer phenomena between the PS and the WOC[6,7]. In this context, covalently-bound molecular PS-WOC dyad systems have proven to be more efficient in photocatalytic WO since the rate of electron transfer from the WOC to the PS is significantly faster[8,9]. Thus, molecular PS-WOC dyad systems based on second and third row transition elements[9,10,11] and

abundant first row elements[12,13] have been successfully employed in photocatalytic WO. Transition from homogeneous to colloidal/heterogeneous species takes place recurrently during WO catalysis[14,15,16], particularly when first row transition metals and/or easily oxidizable ligands are employed[17]. Despite the high activity often shown by these *in situ* formed species, their size, composition and reactivity are poorly controlled. Therefore, the *ex situ* synthesis of metal nanoparticle (NP) catalysts with well-controlled size and surface properties might allow a better tuning of their catalytic performance. In this regard, the WO photocatalytic performance of colloidal dye (PS)-decorated  $\text{IrO}_x$  suspensions has been reported by Mallouk and co-workers[7,8,18]. In these hybrid dyads, the PS serves both as NP stabilizer and light-harvester, thus helping to overcome the thermodynamically unfavorable barrier associated with water oxidation.

Also, Frei and collaborators have reported that the use of electron conducting *p*-oligo(phenylenevinylene) molecular wires covalently bonded to the  $\text{Co}_3\text{O}_4$  core of  $\text{Co}_3\text{O}_4/\text{SiO}_2$  core/shell NPs boost hole injection from oxidized PS molecules either present in solution[19,20] or electrostatically adsorbed onto the  $\text{SiO}_2$  shell[21] to the  $\text{Co}_3\text{O}_4$  core. However, to our knowledge, no examples of WOCs are known so far in which the PS is covalently bound to abundant first row transition metal oxide NPs, which would reduce the global cost of the water splitting process.

Recent literature data thus underline the interest of a rational design of hybrid PS-NP catalysts for the WO reaction. Within this context, the organometallic approach, which is recognized to be highly efficient to prepare NPs with high control over the size, composition and surface properties[22], may offer new opportunities in the synthesis of hybrid PS-NP materials with covalent bonding between the PS and the NP surface. In this way, well-controlled hybrid catalytic materials would be accessible. Eventually, they would permit studies of the influence of the direct link between

the PS and the NP surface on their reactivity, adjusting the dyads to reach better catalytic performances. With this idea in mind, we decided to investigate the grafting of polypyridyl-Ru<sup>II</sup> complexes acting as the PS at the surface of Co<sub>3</sub>O<sub>4</sub> NPs prepared by organometallic chemistry as a strategy to obtain advanced WO photocatalysts. Therefore, herein we report the synthesis and full characterization of novel hybrid PS-NP materials obtained by covalently anchoring light-harvesting [Ru(bpy)<sub>3</sub>]<sup>2+</sup> derived-complexes (bpy = 2,2'-bipyridine) to preformed abundant first row cobalt oxide NPs (Co<sub>3</sub>O<sub>4</sub> NPs), and their use as catalysts in the photoinduced oxidation of water. Their catalytic performance is compared with that of colloidal mixtures of non-bonded PS and Co<sub>3</sub>O<sub>4</sub> NPs, and Co<sub>3</sub>O<sub>4</sub> NPs alone. Finally, flash photolysis/transient absorption methods as well as detailed photochemical analyses are used to gain further insight into the specific processes and rates associated with each component of the catalytic system and thoroughly discussed.

## 2. Results and Discussion

### 2.1. Synthesis and characterization of the nanomaterials

Since the direct synthesis of ultrafine Co<sub>3</sub>O<sub>4</sub> NPs is a challenging process[23], we designed a three-step strategy to obtain the target PS-Co<sub>3</sub>O<sub>4</sub> NPs hybrids: 1) synthesis of Co NPs with an average size of a few nanometers and narrow size distribution; 2) oxidation of these NPs into the target Co<sub>3</sub>O<sub>4</sub> nanomaterial while keeping their morphological features unchanged, and 3) grafting of Ru<sup>II</sup>-polypyridyl complexes with anchoring groups on the surface of the Co<sub>3</sub>O<sub>4</sub> NPs. A

literature survey revealed that to reach Co NPs with an average size of a few nanometers, narrow size distribution and controlled surface chemistry, the reducing agent and metal precursor should be carefully chosen. One of the best precursors in this regard is the organometallic complex [Co(η<sup>3</sup>-C<sub>8</sub>H<sub>13</sub>)(η<sup>4</sup>-C<sub>8</sub>H<sub>12</sub>)], which upon hydrogenation releases only cobalt atoms and cyclooctane, a non-coordinating molecule[24]. This synthetic strategy avoids competition between the introduced stabilizing agent and reaction by-products, observed in other cases. The NPs produced in this way display high reactivity towards air[25,26], even at low temperature, which is a prerequisite to keep the morphological parameters unchanged during the oxidation process and reach Co<sub>3</sub>O<sub>4</sub> NPs of controlled average size and size distribution. To facilitate the eventual grafting of the polypyridyl Ru<sup>II</sup> complexes on the surface of the NPs, the use of strongly coordinating stabilizers like carboxylic acids should be avoided. For this reason, and based on our former work on Ru NPs, 1-heptanol was chosen as solvent and stabilizer for the preparation of Co NPs[27]. Briefly, the synthesis of Co NPs was performed by decomposition of a 1-heptanol solution of the organometallic precursor [Co(η<sup>3</sup>-C<sub>8</sub>H<sub>13</sub>)(η<sup>4</sup>-C<sub>8</sub>H<sub>12</sub>)] under 3 bar of H<sub>2</sub> at room temperature. TEM (Transmission Electron Microscopy) analysis carried out from the so-obtained crude dark-brown colloidal solution revealed the formation of a monodisperse population of spherical NPs of mean size 3.0 ± 0.1 nm (Fig. 1). These particles are well-dispersed on the TEM grid and display a narrow size distribution with a standard deviation below 5% of the mean size.

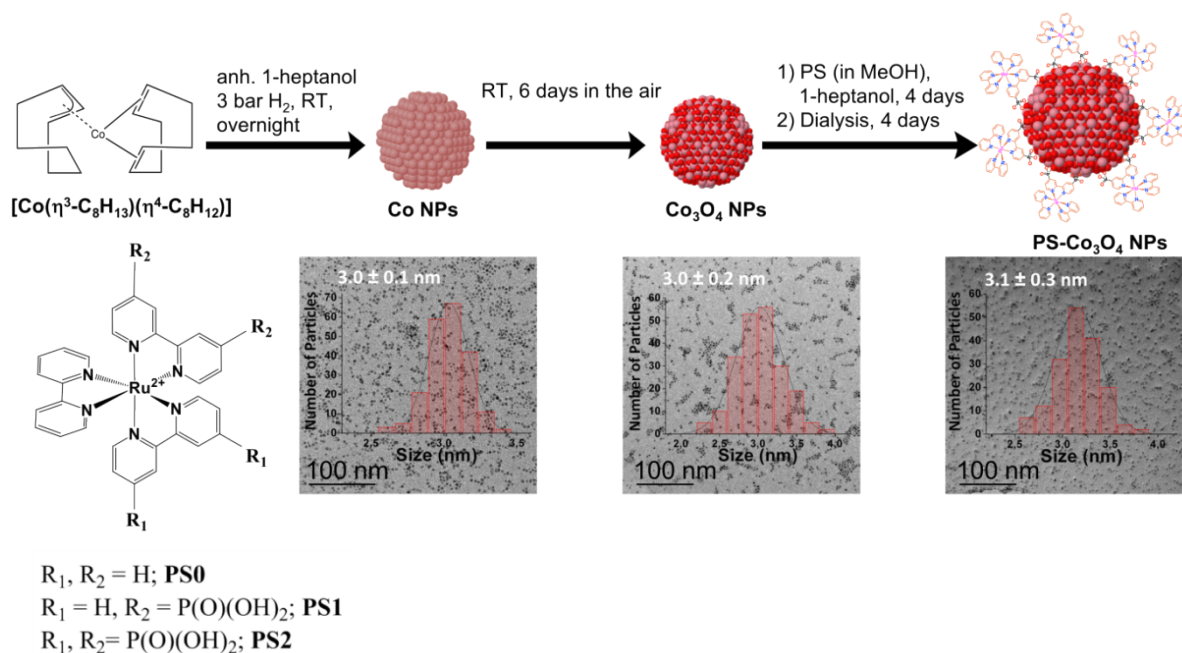


**Fig. 1.** From left to right, synthesis and TEM images of Co, Co<sub>3</sub>O<sub>4</sub> and PS-Co<sub>3</sub>O<sub>4</sub> NPs (PS in the example shown is **PS1**). Bottom left: Schematic drawing of [Ru(bpy)<sub>3</sub>]<sup>2+</sup> (**PS0**) and modified [Ru(bpy)<sub>3</sub>]<sup>2+</sup> complexes with 2 or 4 phosphonic acid coordinating pending groups (**PS1** and **PS2**, respectively) used as photosensitizers.

Recovery of the NPs from the 1-heptanol colloidal solution was performed by application of a magnet on the reactor walls (magnetic filtration). **Successive** washings with pentane followed by drying of the solid under vacuum afforded Co NPs in the form of a black fine powder, which was used for further characterizations. WAXS (Wide-Angle X-Ray Scattering) analysis of the sample confirmed the presence of Co NPs in the α (hcp) and ε (metastable cubic) crystalline structures as evidenced by the good match observed between experimental data and the combination of reference patterns (PDF 01-080-6668 and PDF 04-017-5578, respectively, Fig. 2) and with a coherence length of ca. 2.5 nm (Fig. S1). The Co content in the sample determined by ICP-OES (35.35%) suggests an empirical formula (1-heptanol)<sub>0.9</sub>Co<sub>1</sub> (see Supporting Information) which points to more than one 1-heptanol molecule per surface Co atom, suggesting the formation of interacting multilayers around the NPs.

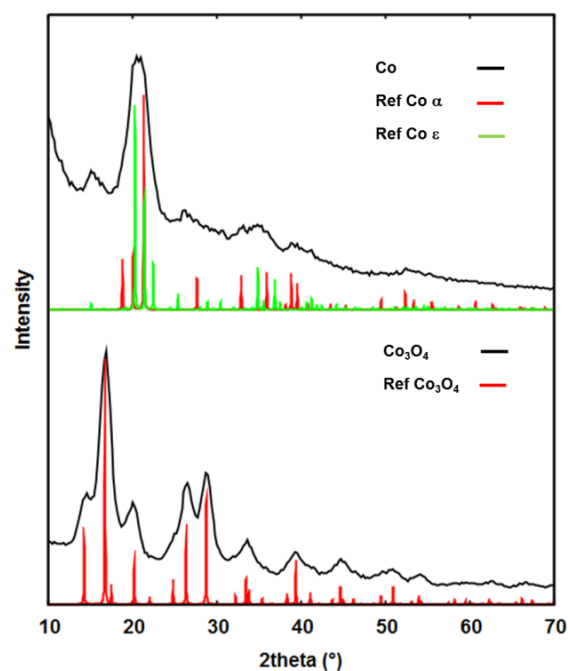


**Fig. 2.** WAXS analysis of Co NPs (top) and Co<sub>3</sub>O<sub>4</sub> NPs (bottom) in comparison with Co α / Co ε and Co<sub>3</sub>O<sub>4</sub> phase diagrams for Co NPs and Co<sub>3</sub>O<sub>4</sub> NPs, respectively.

Complete conversion of the Co NPs previously described into Co<sub>3</sub>O<sub>4</sub> NPs was achieved in **mild** reaction conditions by simple exposure of the particles in the solid state under ambient air for 6 days. The NPs are well dispersed on the TEM images recorded after dissolution of the powder in

1-heptanol, indicating the absence of extended aggregation during the oxidation process. The average size of the final NPs was estimated to be  $3.0 \pm 0.2$  nm (Fig. 1). Taking into account the change in material density ( $8.9 \text{ g}\cdot\text{cm}^{-3}$  for bulk Co compared to  $6.11 \text{ g}\cdot\text{cm}^{-3}$  for bulk  $\text{Co}_3\text{O}_4$ ) one could expect the volume of the NP to double upon oxidation, leading to an expected diameter value of around 3.9 nm. This apparent absence of volume change was already reported for the study of the mild oxidation of Co NPs embedded in a polymer matrix[25]. This can be related to the lower density of the Co oxide NPs, which makes the determination of their exact diameter from TEM images less precise and may induce its systematic underestimation. Oxidation of the CoNPs into  $\text{Co}_3\text{O}_4$  could be confirmed by WAXS, XPS (X-Ray Photoelectron Spectroscopy) analyses and by IR spectroscopy.

WAXS measurements evidenced the presence of nanoparticles displaying a coherence length of ca. 3.0 nm (Fig. S1) and a crystalline structure corresponding to the  $\text{Co}_3\text{O}_4$  phase as shown by the good match observed between experimental data and the reference pattern (PDF 04-005-4386) (Fig. 2).

At first sight, the perfect agreement between the coherence length and the mean size determined by TEM points towards highly crystalline nanoparticles. This is surprising given the mild conditions used during the oxidation of the Co NPs and would rather suggest that the diameter determined from the analysis of the TEM images is underestimated. In XPS (Fig. S2), the  $\text{Co}_3\text{O}_4$  NPs show two main peaks at ca. 780.0 and 795.5 eV, corresponding to the Co  $2p_{3/2}$  and Co  $2p_{1/2}$  components, respectively, accompanied by two broad satellite peaks with very low intensity at higher energies (ca. 788 and 805 eV). According to the literature data, the presence of satellite peaks are an indication of the presence of unpaired electrons in the sample, i.e. the presence of  $\text{Co}^{\text{II}}$  ( $d^7$ ) atoms[28], while both the positions and the intensities of all 4 types of bands observed in the XPS spectrum clearly match the data already reported for the mixed  $\text{Co}^{\text{II}}\text{-Co}^{\text{III}}$  oxide  $\text{Co}_3\text{O}_4$ [28,29].

IR spectroscopy revealed the presence of typical Co-O stretching bands centered at  $666 \text{ cm}^{-1}$  and  $575 \text{ cm}^{-1}$  [30] within the  $\text{Co}_3\text{O}_4$  structure (green line, Fig. 3) confirming the crystallinity and structure of the nanomaterial. Poorly defined absorptions in the  $1600\text{-}1400 \text{ cm}^{-1}$  region could correspond to adsorbed water and carbonate molecules. Taken together these results show the transformation of preformed Co NPs into crystalline  $\text{Co}_3\text{O}_4$  NPs while preventing aggregation and coalescence of the NPs thanks to the use of mild reaction conditions.

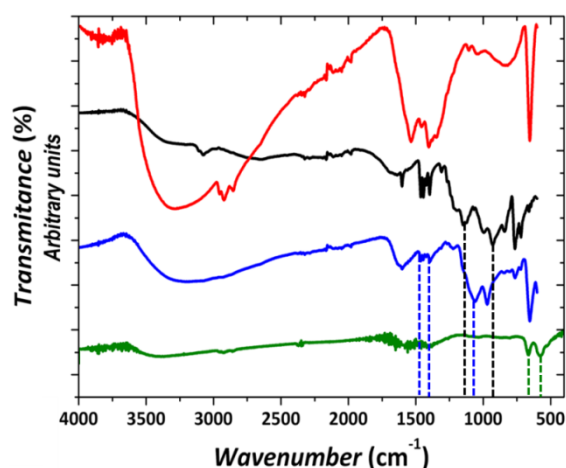


**Fig. 3.** Overlay of ATR-IR spectra of  $\text{Co}_3\text{O}_4$  NPs (red), free **PS1** (black) and **PS1- $\text{Co}_3\text{O}_4$**  NPs hybrid material (blue) and of IR spectrum of a KBr pellet of  $\text{Co}_3\text{O}_4$  NPs (green). The transmittance of each sample has been shifted along the y-axis for comparison purposes. The positions of the bands described along the text have been added as dotted lines.

The next step was the building of the hybrid nanomaterials (**PS- $\text{Co}_3\text{O}_4$**  NPs) by grafting  $\text{Ru}^{\text{II}}$ -polypyridyl complexes at the surface of the  $\text{Co}_3\text{O}_4$  NPs. For this purpose, the  $[\text{Ru}(\text{bpy})_3]^{2+}$  complexes bearing phosphonic acid pending groups (**PS1** with two groups and **PS2** with four groups) were prepared following literature procedures[31,32] (Fig. 1).

The phosphonic acid anchoring group is well known to efficiently interact with metal oxide surfaces[33]. The PS grafting was performed by mixing a 1-heptanol colloidal dispersion of  $\text{Co}_3\text{O}_4$  NPs with a methanol solution of the chosen complex ( $[\text{Ru}^{\text{II}} \text{ complex}]/[\text{Co}_3\text{O}_4 \text{ NPs}] = 0.24$ ) and leaving the obtained reaction mixture under vigorous stirring in the dark for 4 days. The nanohybrid materials were recovered by centrifugation and further purified from unreacted Ru complexes by dialysis against deionized water. This procedure was applied for **PS1** and **PS2** complexes giving rise to the **PS1- $\text{Co}_3\text{O}_4$**  and **PS2- $\text{Co}_3\text{O}_4$**  hybrids, which could be recovered as black powders after evaporation of water under vacuum. From ICP-OES analysis, it can be inferred that these nanomaterials show  $(1\text{-heptanol})_{0.80}(\text{PS1})_{0.09}\text{-Co}_3\text{O}_4$  and  $(1\text{-heptanol})_{0.97}(\text{PS2})_{0.15}\text{-Co}_3\text{O}_4$  empirical formulas (see Supporting Information). The attachment of **PS1** and **PS2** complexes at the surface of the  $\text{Co}_3\text{O}_4$  NPs was attested by ATR-IR spectroscopy (Fig. 3 and Fig. S3, respectively).

As shown in Fig. 3 (black spectrum) the **PS1** complex shows two absorption bands at  $1149 \text{ cm}^{-1}$  and  $928 \text{ cm}^{-1}$  corresponding to the free P=O and P-OH units, respectively[34,35]. The **PS1- $\text{Co}_3\text{O}_4$**



hybrid nanomaterial (Fig. 3, blue spectrum) shows bands in the 1465-1394  $\text{cm}^{-1}$  region, indicative of the presence of the bipyridine backbone of the PS. No free P=O nor P-OH bands are visible, but a band at 1061  $\text{cm}^{-1}$  can be attributed to -P(O-Co) functionalization[35] (by comparison with the 1016  $\text{cm}^{-1}$  value found for -P(O-Zn)<sub>3</sub>), thus supporting the grafting of **PS1** to the surface of Co<sub>3</sub>O<sub>4</sub> NPs and the use of all possible anchoring points. Additionally, neither -CH<sub>3</sub> nor -CH<sub>2</sub>-stretching bands are clearly observed at ca. 2900  $\text{cm}^{-1}$  (such as those seen for Co<sub>3</sub>O<sub>4</sub> NPs (red spectrum) in Fig. 3), indicating that a partial replacement of the 1-heptanol molecules by the **PS1** molecules at the NP surface may have taken place and/or that part of the 1-heptanol initially present could have been released from the NP surface during dialysis. Therefore, we cannot exclude the possible presence of residual 1-heptanol molecules on the surface of the hybrid NPs. TEM analysis from the aqueous colloidal dispersion of the hybrid material revealed the presence of nano-objects with homogeneous shape (spherical) that display a mean size of  $3.1 \pm 0.3$  nm (Fig. 1). The results show that the initial size and morphology of the Co<sub>3</sub>O<sub>4</sub> NPs are maintained after anchoring the **PS1** at their surface. The presence of Ru only in the vicinity of the NPs was evidenced through STEM-EDX analysis, indicating a successful purification process (Fig. S4). The **PS2**-Co<sub>3</sub>O<sub>4</sub> NP hybrid material was characterized accordingly, with very similar results to the **PS1**-Co<sub>3</sub>O<sub>4</sub> hybrid material (Fig. S3, Fig. S5 and Fig. S6). Based on ICP-OES analysis, incorporation of 19 **PS1** and 32 **PS2** complexes per Co<sub>3</sub>O<sub>4</sub> NP is estimated (see Supporting Information for further details). The higher grafting density obtained in the case of the **PS2**-Co<sub>3</sub>O<sub>4</sub> hybrid could be related to the statistically more favored interaction between the surface and the chelating biphosphonate bipyridine ligands.

To sum-up this section, easily obtained Co NPs could be transformed into Co<sub>3</sub>O<sub>4</sub> NPs in mild reaction conditions while preserving their morphology. These results highlight: 1) the efficiency of the synthetic approach, where 1-heptanol acts as both solvent and stabilizer for the preparation of small and size-controlled Co NPs; 2) the possibility to access small Co<sub>3</sub>O<sub>4</sub> NPs by a soft oxidative treatment with a preserved morphology, and 3) the possibility to graft Ru<sup>II</sup>-polypyridyl complexes at the Co<sub>3</sub>O<sub>4</sub> NPs surface, despite the coverage of the surface by 1-heptanol molecules, to get hybrid nanostructured materials with multiple functionalities, namely PS and catalyst. The catalytic properties of the obtained Co<sub>3</sub>O<sub>4</sub> NPs and hybrid PS-Co<sub>3</sub>O<sub>4</sub> NPs materials are described hereafter.

## 2.2. Electrocatalytic behavior in water oxidation catalysis

The electrocatalytic performance of the prepared ultrafine Co<sub>3</sub>O<sub>4</sub> NPs was studied in 1M NaOH solution after their deposition onto a glassy carbon rotating disk electrode (GC-RDE, Fig. S7). The electrode was prepared by depositing three 5  $\mu\text{L}$  drops from a THF dispersion (1 mg of Co<sub>3</sub>O<sub>4</sub> NPs in 250  $\mu\text{L}$  of THF) of the NPs onto the glassy carbon disk of the RDE. Fig. S7a shows the rotating disk voltammetry (RDV) of the as-deposited Co<sub>3</sub>O<sub>4</sub> NPs, where a steep increase in intensity above 0.7 V vs. NHE is visible. This increase in intensity is attributed to the oxidation of water into molecular oxygen[36,37,38], which in our case happens at an onset overpotential ( $\eta$ ) of ca. 0.29 V.

The electrocatalytic performance of our Co<sub>3</sub>O<sub>4</sub> NPs deposited onto GC-RDE was compared with that of other electrocatalysts following the benchmarking methodology reported by Jaramillo *et al.*[36,37,38]. Thus, the electrochemically-active surface area (ECSA) of the Co<sub>3</sub>O<sub>4</sub> modified GC-RDE was estimated to be 0.175  $\text{cm}^2$  from the electrochemical double-layer capacitance ( $C_{dl}$ ) by measuring the non-Faradaic capacitive current associated with double-layer charging from the scan-rate dependence of cyclic voltammograms (CVs)[39,40] over a 0.145-0.245 V vs. NHE potential range (Fig. S9). The roughness factor (RF) was calculated by dividing the estimated ECSA by the geometric area of the electrode, and these factors as well as those corresponding to the electrocatalytic activity of our nanocatalyst are compared with those of the state-of-the-art Co<sub>3</sub>O<sub>4</sub> NPs in the same electrolyte in Table 1. However, it is important to note that the ECSA serves only as an approximate guide for the determination of the RF, since the accuracy of the data lies normally within an order of magnitude[37]. Therefore, comparison with literature data can only be analyzed in terms of general trends. As depicted in Table 1, the Co<sub>3</sub>O<sub>4</sub> modified GC-RDE catalyst reported herein (entry 1) shows an onset overpotential ( $\eta_{\text{onset}}$ ) of ca. 0.29 V vs. NHE, which lies close to the reported values for Co<sub>3</sub>O<sub>4</sub> NPs in graphene[41,42] (entries 3 and 6) and single walled carbon nanotubes (SWCNTs)[43] (entry 7). To achieve a current density of 10  $\text{mA}\cdot\text{cm}^{-2}$ , approximately the current density expected for a 10% efficient solar-to-fuel conversion device[37,44,45,46], a  $\eta_{10\text{mA}/\text{cm}^2}$  of 0.486 V is required (entry 1, this work). This value is close to the  $\eta_{10\text{mA}/\text{cm}^2}$  reported for Co<sub>3</sub>O<sub>4</sub> NPs of similar RF by Jaramillo *et al.*[38] (entry 4) but higher than the  $\eta_{10\text{mA}/\text{cm}^2}$  values published for catalytic systems with nearly two orders of magnitude higher RF[47,48] (entries 2 and 5). Even so, it falls within the reported area of interest for catalyst benchmarking[36,37,38]. Most interestingly, when the current at an  $\eta$  of 0.35 V ( $j_g$ )

is normalized by the ECSA[49,50], a normalized current density ( $j_s$ ) of  $1.04 \text{ mA cm}^{-2}$  is obtained. This value is significantly higher than that reported by Jaramillo *et al.* for their  $\text{Co}_3\text{O}_4$ -based nanocatalyst of similar RF and  $\eta_{10\text{mA/cm}^2}$  (entry 4) and also for all other nanostructured metal oxide

electrocatalysts deposited onto GC-RDE[38]. Thus, the  $\text{Co}_3\text{O}_4$  modified GC-RDE reported herein is very active at low  $\eta$  (0.35 V). The system becomes less competitive at higher overpotentials due to the relatively high slope of the Tafel plot above  $\eta = 0.35 \text{ V}$  (approx.  $100 \text{ mV} \cdot \text{dec}^{-1}$ , Fig. S7b).

**Table 1.** Benchmarking parameters vs. NHE for  $\text{Co}_3\text{O}_4$  NPs in 1 M NaOH and comparison with state-of-the-art data in the same electrolyte.

Entry	Catalyst	ECSA /cm <sup>2</sup>	RF	$\eta_{\text{onset}}/\text{V}$	$\eta_{10\text{mA/cm}^2, t=0}/\text{V}$	$\eta_{10\text{mA/cm}^2, t=1\text{h}}/\text{V}$	$j_{g,\eta=0.35\text{V}}/\text{mA} \cdot \text{cm}^{-2}$	$j_{s,\eta=0.35\text{V}}/\text{mA} \cdot \text{cm}^{-2}$	$\varepsilon$ (%)	Ref.
1	3.0 nm $\text{Co}_3\text{O}_4$ NPs <sup>a</sup>	0.175	2.5	0.29	0.486 <sup>h</sup>	0.480 <sup>h</sup>	2.6	1.04	95 <sup>g</sup>	this work
2	10 nm $\text{Co}_3\text{O}_4$ NPs <sup>b</sup>	429	429	---	0.290	---	ca. 25	ca. 0.06	95	47
3	ca. 10 nm $\text{Co}_3\text{O}_4$ NPs <sup>c</sup>	---	---	0.24	0.313	0.313	ca. 30	---	---	41
4	ca. 70 nm $\text{Co}_3\text{O}_4$ NPs <sup>d</sup>	1.52	7.8	---	0.50	0.51	0.06	0.039	---	38
5	50 nm $\text{Co}_3\text{O}_4$ nanocubes <sup>e</sup>	6.44	91.2	---	0.28	---	ca. 70	ca. 0.77	---	48
6	4-8 nm $\text{Co}_3\text{O}_4$ NPs <sup>f</sup>	---	---	ca. 0.27	0.31	---	ca. 35	---	---	42
7	6 nm $\text{Co}_3\text{O}_4$ NPs <sup>g</sup>	---	---	ca. 0.28	0.593	---	ca. 1.8	---	---	43

<sup>a</sup> Using a GC-RDE; <sup>b</sup> deposited on Ni foam; <sup>c</sup> in graphene nanocomposite; <sup>d</sup> deposited onto GC-RDE; <sup>e</sup> In N-doped graphene nanocomposite; <sup>f</sup> in N-doped graphene deposited onto Ni foam; <sup>g</sup> in SWCNTs; <sup>h</sup> deposited onto an FTO electrode.

Both stability and Faradaic efficiency ( $\varepsilon$ ) are key parameters for a catalyst to be suitable for practical applications in WO catalysis. To analyze them, an FTO electrode was loaded with 15  $\mu\text{L}$  of a dispersion of  $\text{Co}_3\text{O}_4$  NPs (2 mg in 500  $\mu\text{L}$  of 1-heptanol) by spin-coating, and afterwards a poly(methyl methacrylate) (PMMA) layer was added as “gluing” material[51]. The generated FTO/ $\text{Co}_3\text{O}_4$ NPs-PMMA electrode showed onset  $\eta$  of ca. 0.29 V (see Fig. S10b), identical to that of the  $\text{Co}_3\text{O}_4$  NPs on GC-RDE (see Table 1), highlighting the negligible effect of the support used. The FTO/ $\text{Co}_3\text{O}_4$ NPs-PMMA electrode was then held at a constant current density of  $10 \text{ mA} \cdot \text{cm}^{-2}$  in a current-controlled experiment for 1 h in 1M NaOH. As shown in Fig. S10a, the system showed a stable operating potential, changing negligibly from  $\eta_{10\text{mA/cm}^2, t=0\text{h}} = 0.486 \text{ V}$  to  $\eta_{10\text{mA/cm}^2, t=1\text{h}} = 0.480 \text{ V}$  during 1 h (entry 1, Table 1). Comparison of the CV polarization curves measured before and after this current-controlled experiment shows a slight increase in the observed current density after catalytic turnover (Fig. S10b). This global increase in current density is indicative of a certain activation of the Co ions in the  $\text{Co}_3\text{O}_4$  NPs. An increase in the  $\text{Co}^{+3/+4}/\text{Co}^{+2}$  population ratio, as suggested by Frei and co-workers[52], and / or the elimination of 1-heptanol molecules present at the surface of the NPs increasing the number of exposed active sites are plausible reasons for this

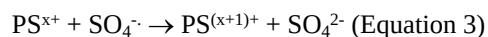
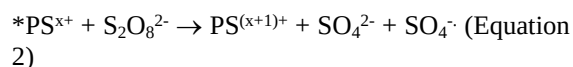
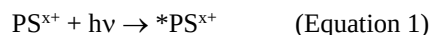
behavior. XPS analysis of the resulting electrode after electrolysis shows the intact composition of the NPs as  $\text{Co}_3\text{O}_4$  (Fig. S11), thus pointing to the removal of 1-heptanol molecules from their surface under catalytic conditions as the origin of the observed activation process. Furthermore, the activation of the NPs does not significantly affect the Tafel slopes (Fig. S10c), which are very similar before and after catalytic turnover. In addition, a Faradaic efficiency of 95% was determined by quantifying the amount of  $\text{O}_2$  generated during a bulk electrolysis (0.886 V vs. NHE corresponding to an initial current density of  $10 \text{ mA} \cdot \text{cm}^{-2}$ ) using an  $\text{O}_2$ -probe and dividing it by the theoretical  $\text{O}_2$  amount calculated from the total charge passed through the system (Fig. S12), thus confirming the production of  $\text{O}_2$  as the only reaction taking place.

### 2.3. Photochemical water oxidation catalysis

The efficiency of the  $\text{Co}_3\text{O}_4$  NPs as a photocatalyst for WO was first evaluated in  $\text{Na}_2\text{SiF}_6\text{-NaHCO}_3$  (0.02-0.04 M, pH 5.60) in the presence of **PS0** ( $[\text{Ru}(\text{bpy})_3]^{2+}$ ) and its phosphonate derivatives **PS1** or **PS2** as photosensitizers (Fig. 1), using sodium peroxodisulfate as the sacrificial electron-acceptor (SEA) and liquid phase Hansatech-type microsenors for measuring the evolved oxygen (Fig. S13, Fig. S14 and Fig. S15). It is noteworthy that the semiconducting  $\text{Co}_3\text{O}_4$  NPs alone do not behave as photocatalysts for this



reaction. The photoactive species responsible for the activation of the Co<sub>3</sub>O<sub>4</sub> NPs in WO is PS<sup>(x+1)+</sup>, which is generated after a three-step process as follows:



The influence of PS concentration on the turnover number (TON) has been studied with **PS1** in order to determine the best [PS]/[Co<sub>3</sub>O<sub>4</sub>(heptanol)<sub>2.8</sub> units] ratio to be used (Fig. S16). The curve (TON vs. **PS1** equiv) obtained reaches a plateau at *ca.* 6.0 equiv of PS. Consequently, a PS:Co<sub>3</sub>O<sub>4</sub>(heptanol)<sub>2.8</sub> units ratio of 6.0:1.0 was chosen for the following photochemical WO studies. As reported in Table 2 (entries 1-3), all the tested PS (Fig. 1) could oxidize the Co<sub>3</sub>O<sub>4</sub> NPs under catalytic conditions. These results are consistent with the electrochemical analysis of the Co<sub>3</sub>O<sub>4</sub> NPs shown above, since their onset potential at pH 5.6 (*ca.* 1.1 V vs. NHE, Fig. S17) is lower than that of the Ru<sup>III</sup>/Ru<sup>II</sup> redox couple for all PS tested (1.2-1.3 V vs. NHE, Fig. S18). TON and TOF (turnover frequency, min<sup>-1</sup>) values were determined from the estimated total number of NPs and of PS molecules present on each sample (as presented in the Supporting Information, these values are underestimated; yet relative values can be obtained). Thus, the TON per NP obtained for the catalytic mixtures made of Co<sub>3</sub>O<sub>4</sub> NPs plus **PS0**, **PS1** or **PS2** are all similar and within the range 453-604 (entries 1, 2, 3 in Table 2). Concerning the TOF per NP, it is reduced by approximately half when doubling the number of phosphonate groups present (67.9 vs. 36.2 min<sup>-1</sup> for **PS1** and **PS2**, respectively; entry 2 vs. entry 3). The TOF per PS is also reduced by a similar amount (0.053 vs. 0.028 min<sup>-1</sup> for **PS1** and **PS2**, respectively). One potential reason for the reduced TOF values for the **PS2** case

could be that the presence of four phosphonate binding groups could allow the simultaneous binding of a single **PS2** unit onto two Co<sub>3</sub>O<sub>4</sub> NPs, thus favoring their aggregation, in contrast to the **PS1** system. This hypothesis is confirmed when comparing the TEM images of the as-synthesized hybrid **PS1**-Co<sub>3</sub>O<sub>4</sub> and **PS2**-Co<sub>3</sub>O<sub>4</sub> systems (Fig. 1 and Fig. S5, respectively), where higher aggregation and lower dispersion of the NPs are obtained for **PS2**-Co<sub>3</sub>O<sub>4</sub>. At this point, it is also worth mentioning that the limiting factors that may stop the O<sub>2</sub> evolution in such photocatalytic systems are usually the degradation of the PS and the pH decrease due to the release of protons during the reaction[53,54,55]. However, it is interesting to note that O<sub>2</sub> evolution was not resumed under our conditions after the addition of an extra aliquot of PS. Thus, some kind of inhibition of the whole photocatalytic system and not only PS degradation takes place. This inhibition could be caused by the progressive increase in the ionic strength of the medium (sulfate ions are produced during catalysis), as this can negatively affect the performance of the NPs due to a reduction of the quenching efficiency of the photoexcited PS (\*PS<sup>x+</sup>) by peroxodisulfate (Equation 2)[56]. In addition, another phenomenon that typically explains the reduced performance of nanocatalysts with time in the presence of the NaSiF<sub>6</sub>-NaHCO<sub>3</sub> buffer is the hydrolysis of the buffer to generate SiO<sub>2</sub> particles, which can provoke the adsorption of the cationic PS molecules onto their surface, thus competing with the catalytic NPs and reducing the global catalytic performance[18]. This last hypothesis has been confirmed by HREM (High Resolution TEM) and STEM (Scanning TEM) analyses of the recovered nanocatalyst after photocatalytic turnover in the presence of **PS1**, in which Co<sub>3</sub>O<sub>4</sub> NP aggregates of *ca.* 50 nm attached to a bigger Si-containing aggregate are observed (Fig. S19).

**Table 2.** TON and TOF ( $\text{min}^{-1}$ ) per NP and per PS obtained as a function of PS nature in photochemical WO measurements with single  $\text{Co}_3\text{O}_4$  NPs and hybrid PS- $\text{Co}_3\text{O}_4$  NPs at pH 5.6.

Entry	System	PS: $\text{Co}_3\text{O}_4$ ratio	TON ( $\text{O}_2/\text{NP}$ )	TOF $\text{min}^{-1}$ ( $\text{O}_2/\text{NP}$ )	TON ( $\text{O}_2/\text{PS}$ )	TOF $\text{min}^{-1}$ ( $\text{O}_2/\text{PS}$ )
1	$\text{Co}_3\text{O}_4$ + PS0	6.0:1.0	453	49.4	0.35	0.038
2	$\text{Co}_3\text{O}_4$ + PS1	6.0:1.0	566	67.9	0.44	0.053
3	$\text{Co}_3\text{O}_4$ + PS2	6.0:1.0	604	36.2	0.47	0.028
4	$\text{Co}_3\text{O}_4$ + PS1	0.09:1.0	< 1	-	< 0.1	-
5	$\text{Co}_3\text{O}_4$ + PS2	0.15:1.0	< 1	-	< 0.1	-
6	PS1- $\text{Co}_3\text{O}_4$	0.09:1.0	5.4	0.90	0.28	0.046
7	PS2- $\text{Co}_3\text{O}_4$	0.15:1.0	82.0	2.05	2.53	0.063

Concerning the **PS1- $\text{Co}_3\text{O}_4$**  and **PS2- $\text{Co}_3\text{O}_4$**  hybrid materials, the number of PS per  $\text{Co}_3\text{O}_4$  NP unit were estimated to be 0.09 and 0.15, respectively (see Supporting Information). Thus, in order to compare the photocatalytic performance of these hybrid dyads with that of the corresponding unbound systems, similar PS /  $\text{Co}_3\text{O}_4$  ratios were applied under catalytic conditions for the two control experiments (Fig. 4). Note that for experiments in which little oxygen is evolved, we observe a decrease of the signal inside the chamber when exposed to light due to the reaction of the PS with residual oxygen traces[57].

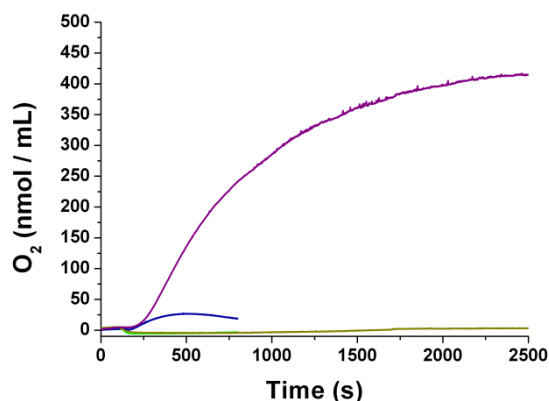


**Fig. 4.** Photocatalytic oxygen production by different  $\text{Co}_3\text{O}_4$ -PS systems. Green line:  $\text{Co}_3\text{O}_4$  NPs ( $9.66 \cdot 10^{-4}$  M) in the presence of **PS1** ( $1.23 \cdot 10^{-4}$  M) and  $\text{Na}_2\text{S}_2\text{O}_8$  ( $7.85 \cdot 10^{-2}$  M). Khaki line:  $\text{Co}_3\text{O}_4$  NPs ( $9.95 \cdot 10^{-4}$  M) in the presence of **PS2** ( $1.05 \cdot 10^{-4}$  M) and  $\text{Na}_2\text{S}_2\text{O}_8$  ( $8.08 \cdot 10^{-2}$  M). Blue line: **PS1- $\text{Co}_3\text{O}_4$**  NPs ( $1.02 \cdot 10^{-3}$  M) in the presence of  $\text{Na}_2\text{S}_2\text{O}_8$  ( $7.32 \cdot 10^{-2}$  M). Purple line: **PS2- $\text{Co}_3\text{O}_4$**  NPs ( $1.09 \cdot 10^{-3}$  M) in the presence of  $\text{Na}_2\text{S}_2\text{O}_8$  ( $7.87 \cdot 10^{-2}$  M). All measurements were performed in  $\text{Na}_2\text{SiF}_6$ - $\text{NaHCO}_3$  (0.02-0.04 M, pH 5.60) buffer solution. Irradiation provided by a Xe lamp equipped with a 400 nm cut-off filter and calibrated to 1 sun ( $100 \text{ mW cm}^{-2}$ ). T =  $25^\circ\text{C}$ .

As shown in Table 2, the oxygen evolved by both unbound systems is almost negligible (entries 4 and 5 and Fig. 4). This can be attributed to the kinetic prevalence of the deactivation processes described above (PS degradation, NP aggregation) competing with oxygen evolution when very low concentrations of unbound PS are used. Conversely, the same PS /  $\text{Co}_3\text{O}_4$  ratio is rather more active when bound PS- $\text{Co}_3\text{O}_4$  hybrid systems are employed (entries 6 and 7). These results could be expected in part if taking into account that in PS-NP dyad systems the electron transfer between both entities is obviously not limited by diffusion, as for the unbound systems. Furthermore, comparison of entries 6 and 7 in Table 2 shows the rather superior activity of **PS2- $\text{Co}_3\text{O}_4$**  (TON and TOF per NP of 82 and  $2.05 \text{ min}^{-1}$ , respectively) versus **PS1- $\text{Co}_3\text{O}_4$**  (TON and TOF per NP of 5.4 and  $0.90 \text{ min}^{-1}$ , respectively). Thus, the superior PS surface functionalization in **PS2- $\text{Co}_3\text{O}_4$**  (32 PS molecules per NP vs. the 19 molecules present in **PS1- $\text{Co}_3\text{O}_4$** ) enhances the kinetics of oxygen evolution and better stabilizes the catalytic system, increasing its durability under photocatalytic conditions (purple line, Fig. 4). When the kinetics of oxygen evolution are normalized by the PS concentration, TOF values of both hybrid systems get closer (right hand column in Table 2, entries 6 and 7), thus confirming the relationship between the rate of photocatalytic turnover and the degree of functionalization of the NPs surface. In terms of stability, the weakness of P-O-M bonds has been extensively identified as a main deactivation pathway of grafted molecular complexes and dye-sensitized systems when employed as catalysts for the oxidation of water[34,35,58]. Thus the higher number of anchoring groups present in **PS2** (4 phosphonate groups vs. 2 present in **PS1**) can also contribute to the superior longevity of the **PS2- $\text{Co}_3\text{O}_4$**  hybrid system.

To further study the fate of the hybrid dyad nanocatalysts under photocatalytic WO conditions,

the crude reaction mixture after a 1h photocatalytic test with **PS1**-Co<sub>3</sub>O<sub>4</sub> and **PS2**-Co<sub>3</sub>O<sub>4</sub> were dialyzed against 2 L of deionized water for 4 days followed by centrifugation and air-drying. Some partial aggregation was observed by TEM analysis (Fig. S20), although less intense than for the non-anchored system (Fig. S19), thus confirming the above proposed protective role of the attached **PS1** molecules against aggregation. Similar studies with Co<sub>3</sub>O<sub>4</sub> NPs stabilized by phosphonate-derived ligands have also shown the preservation of the NP size along light driven WO catalysis[59]. On the other hand, IR spectroscopy showed the loss of **PS1** (Fig. S21), since the intensity of the bpy bands at 1400-1500 cm<sup>-1</sup> and the -P(O-Co) bands at ca. 1060 cm<sup>-1</sup> decreases after photocatalysis. Also, ICP-OES analyses evidence the decrease in the [Ru] / [Co] ratio from 0.03 to 0.003 after catalysis. This 90% loss in PS can be not only due to its decomposition, which is kinetically competitive with the oxidation of water[55], but also to its decoordination from the surface of the Co<sub>3</sub>O<sub>4</sub> NPs, as commonly observed in related systems[34,35,58]. Interestingly, for the **PS2**-Co<sub>3</sub>O<sub>4</sub> system the [Ru] / [Co] ratio only decreased from 0.05 to 0.033 after catalysis (33% loss in PS). The higher stability of the **PS2**-Co<sub>3</sub>O<sub>4</sub> system compared to **PS1**-Co<sub>3</sub>O<sub>4</sub> can only be assigned to the presence of four phosphonate anchoring groups in the former, thus accounting for its superior longevity under photocatalytic conditions.

In summary, the results shown in this section highlight the benefits of the dyad approach where the direct connection between the Co<sub>3</sub>O<sub>4</sub> nanocatalyst and the PS facilitates electron-transfer and stabilizes the system against aggregation under turnover conditions due to the protective effect of the PS at the surface of the Co<sub>3</sub>O<sub>4</sub> NPs. However, they also emphasize the relative instability of the -P(O-Co) bonds under turnover conditions and the need of further research for developing more stable systems with higher durability.

#### 2.4. Photophysical studies

In order to rationalize the kinetics of light induced oxygen evolution described above, and the precise role and contribution of each component in the catalytic systems, a series of steady-state and time-resolved measurements were undertaken.

Indeed, photo-oxidation of different PS upon addition of the electron acceptor peroxodisulfate, according to Equation 2, was investigated by steady-state MLCT luminescence quenching and emission lifetime changes of the inherently luminescent PS in Na<sub>2</sub>SiF<sub>6</sub>-NaHCO<sub>3</sub> 0.02-0.04 M, pH 5.60 (Fig. S22, see Supporting Information for experimental details). Information on the nature of the quenching processes (i.e. static vs dynamic) was

sought via Stern-Volmer (SV) plots, I<sup>0</sup>/I vs. [S<sub>2</sub>O<sub>8</sub><sup>2-</sup>] (where I<sup>0</sup> and I are the emission intensity of the excited PS (\*PS) in the absence and presence of the quencher, respectively) for all PS (alone and attached to Co<sub>3</sub>O<sub>4</sub> NPs), and are shown in Fig. S23.

The SV plots for the **PS1**-Co<sub>3</sub>O<sub>4</sub> and **PS2**-Co<sub>3</sub>O<sub>4</sub> hybrid systems show a linear trend, while for the free PS the SV plots significantly deviate from linearity. These results are similar to those previously reported by Musaev[60] and Bard[61] for [Ru(bpy)<sub>3</sub>]<sup>2+</sup> (**PS0** in our work) and the same quencher in a different electrolyte. They showed that the SV plot is described by a model that takes into account the formation of ground-state ion pairs between the emitter and the quencher. In this case, two different quenching processes can occur: collisional or dynamic quenching (bimolecular pathway) or a static or complex formation quenching (unimolecular pathway)[62,63]. Dynamic quenching occurs when the excited photosensitizer collides with the quencher, following the conventional Stern-Volmer behavior. However, in some cases the photosensitizer can initially form a stable ion-pair complex with the quencher, followed by a photoexcitation of the whole system (Scheme S1). The model that considers both quenching processes at the same time gives rise to the following equation for quenching emission[61]:

$$\frac{I^0}{I} = \frac{(1 + K_{eq}[S_2O_8^{2-}])(1 + k_q\tau_0[S_2O_8^{2-}])}{1 + \frac{\tau_0}{\tau'} \frac{(K_{eq}[S_2O_8^{2-}](1 + k_q\tau_0[S_2O_8^{2-}]))}{(1 + k_q'\tau'[S_2O_8^{2-}])}} \quad (\text{Equation 4})$$

where K<sub>eq</sub> is the equilibrium constant of ion pair formation, and the unquenched unimolecular decay time and the bimolecular quenching constant of the excited emitter in the free form are, respectively, τ<sub>0</sub> and k<sub>q</sub>, while in ion pair state are τ' and k<sub>q</sub>'. Under conditions of negligible ion-pair formation, K<sub>eq</sub>[S<sub>2</sub>O<sub>8</sub><sup>2-</sup>] << 1, that is, under dynamic (or bimolecular) quenching, Equation 4 is simplified to the Stern-Volmer equation:

$$\frac{I^0}{I} = \frac{\Phi_{Ar}}{\Phi} = \frac{\tau_0}{\tau} = 1 + k_q\tau_0[S_2O_8^{2-}] \quad (\text{Equation 5})$$

while for K<sub>eq</sub>[S<sub>2</sub>O<sub>8</sub><sup>2-</sup>] >> 1, that is, under static (or unimolecular) quenching

$$\frac{I^0}{I} = \frac{1 + k_q\tau_0[S_2O_8^{2-}]}{\left(\frac{\tau_0}{\tau'}\right)(1 + k_q\tau_0[S_2O_8^{2-}])(1 + k_q'\tau'[S_2O_8^{2-}])^{-1}} \quad (\text{Equation 6})$$

and when k<sub>q</sub>'τ'[S<sub>2</sub>O<sub>8</sub><sup>2-</sup>] in the denominator is large compared to 1, then

$$\frac{I^0}{I} = \frac{\tau_0}{\tau'} + k_q'\tau'[S_2O_8^{2-}] \quad (\text{Equation 7})$$

As shown in Fig. S23, data for **PS1**-Co<sub>3</sub>O<sub>4</sub> and **PS2**-Co<sub>3</sub>O<sub>4</sub> fit well into Equation 5, suggesting that the equilibrium constant corresponding to the formation of an S<sub>2</sub>O<sub>8</sub><sup>2-</sup>/PS-Co<sub>3</sub>O<sub>4</sub> ion pair is negligible and most quenchers are not in the ion-

pair ground-state. Thus, the quenching proceeds through a bimolecular pathway. On the contrary, for all free PS there is a deviation from linearity of the SV plots at  $[S_2O_8^{2-}] < 15$  mM, which indicates the formation of a ground-state ion pair between PS and  $S_2O_8^{2-}$ . Assuming that  $k_q$  and  $k_q'$  are similar[61], these SV plots can be fitted by Equation 4, and the results of all fittings are listed in Table 3. Also, the SV plots of **PS0**, at  $[S_2O_8^{2-}] >$

50 mM show a change in the curvature, with an extrapolated intercept at the x axis origin away from (0,1) (Fig. S23), which suggests that adsorption of the cationic PS to negatively charged silica particles (originated from  $Na_2SiF_6$  hydrolysis)[18] or dynamic quenching processes are taking place as a result of the increased ionic strength[61,64,65].

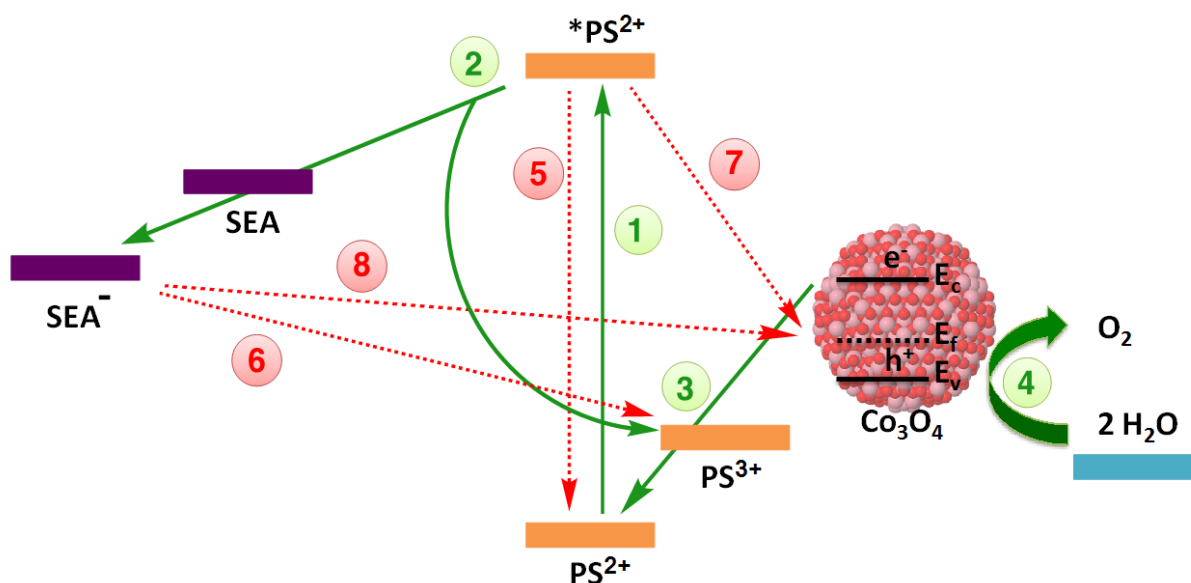
**Table 3.** Results of kinetic analysis of the  $\{PS^*, S_2O_8^{2-}\}$  and  $\{Co_3O_4-PS^*, S_2O_8^{2-}\}$  systems at pH 5.6.

Entry	System	$\Phi_{O_2}^a$	$\Phi_{Ar}^b$	$\tau_{Ar0},^c$ ns	$\tau_{O_20},^d$ ns	$\tau_{NP50},^e$ ns	$\tau',^f$ ns	$\tau_0/\tau',^g$	$k_q (k_q'),^h$ $mol^{-1} \cdot L \cdot s^{-1}$	$K_{eq},^i$ $mol \cdot L^{-1}$	$k_{ET},^j$ $s^{-1}$	$k_q[S_2O_8^{2-}],^k$ $s^{-1}$	$k_q[S_2O_8^{2-}],^l$ $s^{-1}$
1	<b>PS0</b> no buffer	0.028	0.042	550	366	N/A	108	5.09	$3.9 \cdot 10^8$	$6.93 \cdot 10^2$	$7.4 \cdot 10^6$	$1.17 \cdot 10^8$	$7.41 \cdot 10^6$
2	<b>PS0</b>	0.021	0.032	558	364	550	55	10.22	$4.39 \cdot 10^8$	$2.46 \cdot 10^2$	$1.65 \cdot 10^7$	$1.32 \cdot 10^8$	$8.34 \cdot 10^6$
5	<b>PS1</b>	0.026	0.031	501	420	512	109	4.59	$3.17 \cdot 10^7$	$1.29 \cdot 10^2$	$7.17 \cdot 10^6$	$9.52 \cdot 10^6$	$6.02 \cdot 10^5$
6	<b>PS2</b>	0.023	0.029	429	340	425	312	1.37	$7.50 \cdot 10^7$	$2.81 \cdot 10^1$	$8.72 \cdot 10^5$	$2.25 \cdot 10^7$	$1.43 \cdot 10^6$
7	<b>PS1- Co<sub>3</sub>O<sub>4</sub></b>	0.025	0.030	497	414	497	-	-	$5.05 \cdot 10^7$	-	-	$1.52 \cdot 10^7$	$9.60 \cdot 10^5$
8	<b>PS2- Co<sub>3</sub>O<sub>4</sub></b>	0.022	0.030	412	327	412	-	-	$1.94 \cdot 10^7$	-	-	$5.82 \cdot 10^6$	$3.69 \cdot 10^5$

<sup>a</sup> Quantum yield in air-saturated buffer solutions in the absence of quencher; <sup>b</sup> quantum yield in argon-saturated buffer solutions in the absence of quencher; <sup>c</sup> from lifetime measurements in the absence of  $S_2O_8^{2-}$  in an argon-saturated buffer solution; <sup>d</sup> from lifetime measurements in the absence of  $S_2O_8^{2-}$  in an air-saturated buffer solution; <sup>e</sup> from lifetime measurements in the absence of  $S_2O_8^{2-}$  in an argon-saturated buffer solution in the presence of  $Co_3O_4$  NPs; <sup>f</sup> calculated from intercept of SV plots ( $\tau_0/\tau'$ ) and  $\tau_0$ ; <sup>g</sup> intercept of SV plots at variable  $[S_2O_8^{2-}]$ ; <sup>h</sup> from slope of SV plots at variable  $[S_2O_8^{2-}]$ ; <sup>i</sup> computational best fit to Equation 4 (see text); <sup>j</sup> Calculated from Equation 8 (see text); <sup>k</sup> Calculated for 0.3 M  $S_2O_8^{2-}$ ; <sup>l</sup> Calculated for 0.019 M  $S_2O_8^{2-}$ .

Data gathered in Table 3 shows that the quantum yield  $\Phi$  (the ratio between emitted photons and absorbed photons) in the presence of oxygen ( $\Phi_{O_2}$ ) is lower than in the presence of Ar ( $\Phi_{Ar}$ ) because of the luminescence quenching effect of oxygen in the former case. Accordingly, lifetimes in the presence of  $O_2$  ( $\tau_{O_20}$ ) are shorter than in the presence of Ar ( $\tau_{Ar0}$ ). Moreover, the similarity of  $\Phi_{Ar}$  in the free and hybrid systems (entries 5,6 vs. 7,8) indicates that no direct electron transfer process exists between the excited PS and the

$Co_3O_4$  NPs in the hybrid systems. Adding  $Co_3O_4$  NPs to the buffered solutions containing the different PS and measuring luminescence lifetimes in the presence of Ar ( $\tau_{NP50}$ ) allowed testing of the significance of charge transfer between \*PS and  $Co_3O_4$  NPs (processes 3 and 7 in Scheme 1). As shown in Table 3, no significant differences are observed between  $\tau_{Ar0}$  and  $\tau_{NP50}$ . Thus, we can assume that no direct interactions occur between the \*PS and free  $Co_3O_4$  NPs.



**Scheme 1.** Scheme of pertinent processes leading to photoinduced water oxidation using prototype dye-sensitized cobalt oxide NPs in a photoelectrochemical system along with main energy levels and relevant desired (in green) and undesired (in red) electron transfer processes. (1) Dye photoexcitation; (2) electron injection/electron acceptor reduction; (3) hole injection/catalyst oxidation; (4) water oxidation; (5) dye (radiative or nonradiative) deexcitation; (6) electron-hole recombination to the oxidized dye; (7) oxidative dye excited-state quenching by the catalyst; (8) electron-hole recombination to the oxidized catalyst. Note that for the sake of simplicity the position of the different species along the y-axis does not necessarily correspond to their energy level. A qualitative representation of the band structure of  $\text{Co}_3\text{O}_4$  NPs is shown. Legend:  $E_v$  (Valence band level),  $E_f$  (Fermi band level),  $E_c$  (Conduction band level) [66].

On the other hand, the intrinsic radiative and non-radiative rate constants of  $\{\text{PS}\cdots\text{S}_2\text{O}_8^{2-}\}^*$  ion pairs should be similar to those of the  $^*\text{PS}$  due to the weak (a few kilocalories per mole) electrostatic interaction between  $\text{PS}$  and  $\text{S}_2\text{O}_8^{2-}$ [60]. Then, the photoinduced unimolecular electron transfer (ET) rate ( $k_{\text{ET}}$ ) can be estimated according to Equation 8, where  $\tau$  is the observed lifetime and  $\tau_0$  is the unquenched lifetime.

$$k_{\text{ET}} = \frac{1}{\tau} - \frac{1}{\tau_0} \quad (\text{Equation 8})$$

At 0.3 M concentration of  $\text{S}_2\text{O}_8^{2-}$ , the bimolecular ET rates  $k_q[\text{S}_2\text{O}_8^{2-}]$  are faster than the unimolecular ET rates ( $k_{\text{ET}}$ ) for all systems at pH 5.6 (Table 3), suggesting that at this concentration  $\text{S}_2\text{O}_8^{2-}$  deactivates the unimolecular quenching process since it inhibits the formation of the ground-state  $\{\text{PS}\cdots\text{S}_2\text{O}_8^{2-}\}$  ion pairs[60]. However, under catalytic conditions (0.019 M  $\text{S}_2\text{O}_8^{2-}$ , last column in Table 3) the bimolecular quenching is basically favored for **PS2** ( $k_q[\text{S}_2\text{O}_8^{2-}] \geq k_{\text{ET}}$ ), whereas the unimolecular quenching is preferential for **PS0** and **PS1** ( $k_{\text{ET}} > k_q[\text{S}_2\text{O}_8^{2-}]$ ).

For all systems, their photo-oxidation by  $\text{S}_2\text{O}_8^{2-}$  has also been studied at pH 8.4, in which **PS1** and **PS2** are deprotonated (Table S1, Fig. S24 and Fig. S25). Under these conditions we can see no

deviations from linearity for the Stern-Volmer plots, since the unimolecular ET mechanism is clearly disfavored now due to the repulsion that appears between the negatively charged  $\text{PS}$  and  $\text{S}_2\text{O}_8^{2-}$  at basic pH. On the other hand, the same Stern-Volmer behavior at pH 5.6 is observed at pH 8.4 for **PS0** since **PS0** is not affected by pH.

Transient absorption spectroscopy was also used to study the difference between the free **PS1** and the **PS1-Co<sub>3</sub>O<sub>4</sub>** hybrid systems. No significant differences were observed between the free  $\text{PS}$  and that attached to  $\text{Co}_3\text{O}_4$  NPs (Fig. S26), and in both cases the ground-state bleaching of **PS1** at 452 nm and the formation of the **PS1\*** excited state near 360 nm could be observed (Fig. S27). Thus, direct charge transfer from the  $\text{Co}_3\text{O}_4$  NPs to **PS1\*** is not observed in any system, as otherwise deduced from the comparison between  $\tau_{\text{A}0}$  and  $\tau_{\text{NP}0}$  (Table 3), meaning that **PS1\*** remains excited until its reaction with the sacrificial electron acceptor  $\text{S}_2\text{O}_8^{2-}$  in agreement with luminescence analyses, and in accordance with Scheme 1.

### 3. Conclusions

In conclusion, we have demonstrated that 1-heptanol serves as both an effective solvent and stabilizing agent for the synthesis of ultra-small Co NPs (ca. 3 nm), preventing their aggregation. The



Co NPs have been oxidized into Co<sub>3</sub>O<sub>4</sub> NPs by air-exposure in mild conditions preserving their morphology and dispersion. When deposited at the surface of a GC-RDE electrode and in 1M NaOH, these Co<sub>3</sub>O<sub>4</sub> NPs electrocatalytically oxidize water with an onset  $\eta$  of ca. 0.29 V and  $\eta_{10\text{mA}/\text{cm}^2}$  of 0.486 V, showing ECSA normalized current densities ( $j_s$ ) of 1.04 mA cm<sup>-2</sup> at  $\eta$  = 0.35 V, a value that outperforms that of all benchmarked nanostructured metal oxide electrocatalysts deposited onto GC-RDE. Despite being stable and showing 95% Faradaic efficiency, the system is less competitive at higher current densities due to its Tafel slope of ca. 100 mV·dec<sup>-1</sup> at  $\eta$  > 0.35 V.

Ru<sup>II</sup> photosensitizers displaying phosphonic acid pending groups (**PS1** with two and **PS2** with four) were attached to the surface of Co<sub>3</sub>O<sub>4</sub> NPs, yielding PS-Co<sub>3</sub>O<sub>4</sub> hybrid systems with a different degree of surface functionalization, namely incorporation of ca. 19 **PS1** and 32 **PS2** complexes per Co<sub>3</sub>O<sub>4</sub> NP. The capacity of these dyad systems to photo-oxidize water into oxygen using visible light and S<sub>2</sub>O<sub>8</sub><sup>2-</sup> as sacrificial electron acceptor at pH 5.6 was evaluated and the results compared with those of unbound systems of the same components and concentrations. The benefits of the dyad approach arise when observing the inactivity of the unbound Co<sub>3</sub>O<sub>4</sub>/PS systems with regards to the significant TON and TOF values per NP (5.4 / 0.90 min<sup>-1</sup> and 82 / 2.05 min<sup>-1</sup>) obtained for **PS1**-Co<sub>3</sub>O<sub>4</sub> and **PS2**-Co<sub>3</sub>O<sub>4</sub>, respectively. The better catalytic performance of the latter over the former was attributed to the higher surface functionalization of **PS2**-Co<sub>3</sub>O<sub>4</sub>, which enhances the kinetics of WO and protects better the catalytic entity under working conditions against aggregation. These data stress the important role of the direct connection between the PS and the nanocatalyst by: 1) favoring their efficient electronic communication with respect specifically to process 3 in Scheme 1, which allows being kinetically-competitive with the typical side deactivation processes of light-driven WO; and 2) minimizing catalyst aggregation under turnover conditions thanks to the protective / stabilizing effect of the PS coordinated at the surface of the Co<sub>3</sub>O<sub>4</sub> NPs. Photophysical measurements show the determinant roles of the sacrificial electron acceptor, diffusion and ground state acceptor-PS complexes, and lack of direct electron transfer between NPs and \*PS.

In summary, this work opens the way towards precisely defined first row PS-NP hybrid dyads by means of the so-called organometallic approach as synthetic methodology, which provides well-controlled and fully characterized cobalt, cobalt oxide and RuPS-Co<sub>3</sub>O<sub>4</sub> nanomaterials. The latter species have proven capable to photo-oxidize water into dioxygen at pH 5.6, being fairly superior to their unbound Co<sub>3</sub>O<sub>4</sub> NPs / PS counterparts under

identical conditions. Therefore, the fine-tuning of this system through the length and nature of the PS-Co<sub>3</sub>O<sub>4</sub> NPs connection is expected to lead to a better understanding of the key parameters governing the catalytic process and is already under way in our laboratories.

## 4. Experimental Section

### 4.1. General

All procedures concerning the synthesis and preparation of samples for characterization of Co nanoparticles were carried out using standard Schlenk tubes, Fisher-Porter glassware and vacuum line techniques or in a glove-box (Braun) under an argon atmosphere. Reagents and solvents were degassed before use via a multi-cycle freeze-pump-thaw process. The (cyclooctadienyl)(1,5-cyclooctadiene)cobalt(I) complex, [Co( $\eta^3$ -C<sub>8</sub>H<sub>13</sub>)( $\eta^4$ -C<sub>8</sub>H<sub>12</sub>)], was purchased from Nanomeps-Toulouse. 1-Heptanol, sodium persulfate, sodium hydroxide, sodium hexafluorosilicate, and sodium bicarbonate were acquired from Sigma-Aldrich. Hydrogen and argon were purchased from Alphagaz. 1-Heptanol was dried over activated molecular sieves (4 Å) prior to use and other reagents were employed as received unless otherwise specified. Solvents (THF, pentane, dichloromethane, diethyl ether) were purified before use by filtration on adequate alumina columns in a purification apparatus (MBraun) and handled under argon atmosphere.

### 4.2. Synthesis protocols

**Photosensitizers:** The photosensitizers used in this work (see Fig. 1) were prepared according to literature data[31,32] and obtained with Cl<sup>-</sup> as counterion.

**Co nanoparticles:** [Co( $\eta^3$ -C<sub>8</sub>H<sub>13</sub>)( $\eta^4$ -C<sub>8</sub>H<sub>12</sub>)] (120 mg, 0.43 mmol) as cobalt source and anhydrous 1-heptanol (20 mL) as both solvent and stabilizer were mixed into a Fisher-Porter reactor under an argon atmosphere inside a glove-box, leading to a brownish solution. Then, the Fisher-Porter reactor was pressurized with 3 bar of H<sub>2</sub> and the reaction mixture was kept under vigorous stirring overnight, after which a dark colloidal dispersion was obtained. Excess H<sub>2</sub> was eliminated under vacuum. A TEM grid was prepared under argon for TEM analysis of the crude colloidal solution. The application of a magnet on the reactor walls allowed to attract the Co NPs as a solid and then to isolate them from 1-heptanol, which was then removed via cannula. The Co NPs were then washed with degassed anhydrous pentane (4 x 20 mL) and dried under vacuum. ICP-OES (wt%): Co (35.35%).



**Co<sub>3</sub>O<sub>4</sub> nanoparticles:** Co<sub>3</sub>O<sub>4</sub> NPs were prepared by treatment of isolated Co NPs under ambient air at room temperature during 6 days. Estimated Co content: 31.33%.

**PS-Co<sub>3</sub>O<sub>4</sub> NP hybrids:** A solution of **PS1** (11 mg, 0.014 mmol, 0.24 eq) or **PS2** (13 mg, 0.014 mmol, 0.24 eq) in methanol (0.4 mL) was added to a colloidal dispersion of Co<sub>3</sub>O<sub>4</sub> NPs (33 mg, 0.058 mmol of Co<sub>3</sub>O<sub>4</sub>(heptanol)<sub>2.8</sub> units) in 1-heptanol (0.6 mL). The reaction mixture was kept under vigorous stirring for 4 days in the dark. Then, precipitation of the crude product was achieved by adding isopropanol (1.5 mL) and diethyl ether (10 mL) and centrifuging at 1000 rpm for 10 min. The obtained crude product and water (1 mL) were introduced in a cellulose membrane bag for dialysis against deionized water (2 L). Dialysis was pursued until the external dialysis solution remained colorless. Then, centrifugation allowed to recover a solid, which was washed 3 times with a mixture of diethyl ether / isopropanol (8:2, v/v) to remove water and 3 times again with diethyl ether before drying under vacuum. The Ru/Co ratio of the obtained PS-Co<sub>3</sub>O<sub>4</sub> NPs hybrids was calculated from ICP-OES measurements. PS-Co<sub>3</sub>O<sub>4</sub> NPs hybrids were stored in the dark. ICP-OES (wt%): **PS1**-Co<sub>3</sub>O<sub>4</sub>, Ru (2.23%), Co (43.60%); **PS2**-Co<sub>3</sub>O<sub>4</sub>, Ru (3.12%), Co (35.22%). Recovered: 19 mg for **PS1**-Co<sub>3</sub>O<sub>4</sub>; 18 mg for **PS2**-Co<sub>3</sub>O<sub>4</sub>.

#### 4.3. Preparation of electrodes

**RDE/Co<sub>3</sub>O<sub>4</sub> and GC/Co<sub>3</sub>O<sub>4</sub> NPs:** 15 µL of a dispersion of Co<sub>3</sub>O<sub>4</sub> NPs (1 mg) in THF (250 µL) were deposited onto the 0.07 cm<sup>2</sup> glassy carbon

(GC) disk from the rotatory disk electrode (RDE) or onto a GC electrode and let it dry under air.

**FTO/Co<sub>3</sub>O<sub>4</sub> NPs-PMMA:** A dispersion of Co<sub>3</sub>O<sub>4</sub> NPs (2 mg) in 1-heptanol (500 µL) was prepared. Then, the NPs were deposited by spin-coating 15 µL of this dispersion onto an FTO electrode followed by evaporation of the solvent in a furnace at 100°C for 10 min. After that, the FTO/Co<sub>3</sub>O<sub>4</sub> NPs electrode was dipped into a 0.5% wt PMMA dichloromethane solution for a few seconds (<10 sec) and air-dried.

**PMMA Coating.** A poly(methyl methacrylate) (PMMA) coating was formed onto the FTO electrode supporting Co<sub>3</sub>O<sub>4</sub> NPs by simply dipping this electrode in dichloromethane (DCM) with 0.5 % wt concentration of PMMA. After soaking the electrode in the PMMA solution for a few seconds (< 10 sec), the electrode was air-dried.

#### Acknowledgements

J. De T. acknowledges the *Universitat Autònoma de Barcelona* for a PIF doctoral grant. Financial supports were provided by MINECO / FEDER (CTQ2015-64261-R and CTQ2015-65268-C2-1-P), IDEX UNITI Emergence (UFTMIP: 2015-209-CIF-D-DRD-127185) and CNRS. GDRI HC3A CNRS action (Catalunya / Midi-Pyrénées) and CTP regional action (Catalunya / CTP2013-00016, Midi-Pyrénées / n°13053026, Basque Country/CTP2013-R03 and Région Aquitaine / n°13010761) are gratefully acknowledged for exchange funding between the partners. J.G.-A. acknowledges the Serra Hùnter Program.

## References

---

- [1] S. Berardi, S. Drouet, L. Francàs, C. Gimbert-Suriñach, M. Guttentag, C. Richmond, T. Stoll, A. Llobet, *Chem. Soc. Rev.* 43 (2014) 7501-7519.
- [2] R. Bofill, J. García-Antón, L. Escriche, X. Sala, A. Llobet, Water Oxidation, in: J. Reedijk, K. Poeppelmeier (Eds.), *Comprehensive Inorganic Chemistry*, II, Elsevier, 2013, Vol 8, pp. 505-523.
- [3] R. Bofill, J. García-Antón, L. Escriche, X. Sala, *J. Photochem. Photobiol. B: Biol.* 152 (2015) 71-81.
- [4] N.S. Lewis, *Science* 351 (2016) aad19201.
- [5] M.D. Kärkäs, O. Verho, E.V. Johnston, B. Akermark, *Chem. Rev.* 114 (2014) 11863-12001.
- [6] B. Limburg, E. Bouwman, S. Bonnet, *ACS Catal.* 6 (2016) 5273-5284.
- [7] W.J. Youngblood, S.-H.A. Lee, Y. Kobayashi, E.A. Hernandez-Pagan, P.G. Hoertz, T.A. Moore, A.L. Moore, D. Gust, T.E. Mallouk, *J. Am. Chem. Soc.* 131(2009) 926-927.
- [8] J. Youngblood, S.H. Lee, K. Maeda, T.E. Mallouk, *Acc. Chem. Res.* 42 (2009) 1966-1973.
- [9] D.L. Ashford, M.K. Gish, A.K. Vannucci, M.K. Brennaman, J.L. Templeton, J.M. Papanikolas, T.J. Meyer, *Chem. Rev.* 115 (2015) 13006-13049.
- [10] N. Kaveevivitchai, R. Chitta, R. Zong, M. El Ojaimi, R.P. Thummel, *J. Am. Chem. Soc.* 134 (2012) 10721-10724.
- [11] H. Li, F. Li, B. Zhang, X. Zhou, F. Yu, L. Sun, *J. Am. Chem. Soc.* 137 (2015) 4332-4335.
- [12] A.M. Lopez, M. Natali, E. Pizzolato, C. Chiorboli, M. Bonchio, A. Sartorel, F. Scandola, *Phys.Chem. Chem. Phys.* 16 (2014) 12000-12007.
- [13] E.A. Karlsson, B.-L. Lee, R.-Z. Liao, T. Akermark, M.D. Kärkäs, V.S. Becerril, P.E.M. Siegbahn, X. Zou, M. Abrahamsson, B. Akermark, *ChemPlusChem* 79 (2014) 936-950.
- [14] R.K. Hocking, R. Brimblecombe, L.-Y. Chang, A. Singh, M.H. Cheah, C. Glover, W.H. Casey, L. Spiccia, *Nat. Chem.* 3 (2011) 461-466.
- [15] M.W. Kanan, D.G. Nocera, *Science* 321 (2008) 1072-1075.
- [16] H.-Y. Wang, J. Liu, J. Zhu, S. Styring, S. Ott, A. Thapper, *Phys. Chem. Chem. Phys.* 16 (2014) 3661-3669.
- [17] P. Garrido-Barrios, C. Gimbert-Suriñach, R. Matheu, X. Sala, A. Llobet, *Chem. Soc. Rev.* 46 (2017) 6088-6098.
- [18] P.G. Hoertz, Y.-I. Kim, W.J. Youngblood, T.E. Mallouk, *J. Phys. Chem. B* 111 (2007) 6845-6856.
- [19] H.S. Soo, A. Agiral, A. Bachmeier, H. Frei, *J. Am. Chem. Soc.* 134 (2012) 17104-17116.
- [20] A. Agiral, H.S. Soo, H. Frei, *Chem. Mater.* 25 (2013) 2264 -2273.
- [21] E. Edri, J.K. Cooper, I.D. Sharp, D.M. Guldi, H. Frei, *J. Am. Chem. Soc.* 139 (2017) 5458-5466.
- [22] C. Amiens, B. Chaudret, D. Ciuculescu-Pradines, V. Collière, K. Fajerwerg, P. Fau, M. Kahn, A. Maisonnat, K. Philippot, *New J. Chem.* 37 (2013) 3374-3401.
- [23] M. Salavati-Niasari, A. Khansari, *CR. Chimie* 17 (2014) 352-358.
- [24] J. Osuna, D. de Caro, C. Amiens, B. Chaudret, E. Snoeck, M. Respaud, J.-M. Broto, A. Fert, *J. Phys. Chem.* 100 (1996) 14571-14574.
- [25] M. Verelst, T.O. Ely, C. Amiens, E. Snoeck, P. Lecante, A. Mosset, M. Respaud, J.-M. Broto, B. Chaudret, *Chem. Mater.* 11 (1999) 2702-2708.
- [26] C. Amiens, *Faraday Discuss.* 125 (2004) 293-309.
- [27] K. Pelzer, K. Philippot, B. Chaudret, *Z. Phys. Chem.* 217 (2003) 1539-1547.
- [28] M.C. Biesinger, B.P. Payne, A.P. Grosvenor, L.W.M. Lau, A.R. Gerson, R.St.C. Smart, *Appl. Surf. Sci.* 257 (2011) 2717-2730.
- [29] J. Yang, H. Lu, W.N. Martens, R.L. Frost, *J. Phys. Chem. C* 114 (2010) 111-119.
- [30] J. Jiang, L. Li, *Materials Letters* 61 (2007) 4894-4896.
- [31] M.R. Norris, J.J. Concepcion, C.R.K. Glasson, Z. Fang, A.M. Lapidés, D.L. Ashford, J.L. Templeton, T.J. Meyer, *Inorg. Chem.* 52 (2013) 12492-12501.
- [32] P. Jansa, O. Baszczyński, E. Procházková, M. Dračinský, Z. Janeba, *Green Chem.* 14 (2012) 2282-2288.
- [33] S.A. Paniagua, A.J. Giordano, O'Neil L. Smith, S. Barlow, H. Li, N.R. Armstrong, J.E. Pemberton, J.-L. Brédas, D. Ginger, S.R. Marder, *Chem. Rev.* 12 (2016) 7117-7158.

- 
- [34] G. Guerrero, P.H. Mutin, A. Vioux, *Chem. Mater.* 13 (2001) 4367-4373.
- [35] G. Guerrero, J.G. Alauzun, M. Granier, D. Laurencin, P.H. Mutin, *Dalton Trans.* 42 (2013) 12569-12585.
- [36] C.C.L. McCrory, S. Jung, I.M. Ferrer, S.M. Chatman, J.C. Peters, T.F. Jaramillo, *J. Am. Chem. Soc.* 137 (2015) 4347-4357.
- [37] C.C.L. McCrory, S. Jung, J.C. Peters, T.F. Jaramillo, *J. Am. Chem. Soc.* 135 (2013) 16977-16987.
- [38] S. Jung, C.C.L. McCrory, I.M. Ferrer, J.C. Peters, T.F. Jaramillo, *J. Mater. Chem. A* 4 (2016) 3068-3076.
- [39] S. Trasatti, O.A. Petrii, *Pure Appl. Chem.* 63 (1991) 711-734.
- [40] J.D. Benck, Z. Chen, L.Y. Kuritzky, A.J. Forman, T.F. Jaramillo, *ACS Catal.* 2 (2012) 1916-1923.
- [41] Y. Zhao, S. Chen, B. Sun, D. Su, X. Huang, H. Liu, Y. Yan, K. Sun, G. Wang, *Sci. Rep.* 5 (2015) 7629, DOI: 10.1038/srep07629.
- [42] Y. Liang, Y. Li, H. Wang, J. Zhou, J. Wang, T. Regier, H. Dai, *Nat. Mater.* 10 (2011) 780-786.
- [43] J. Wu, Y. Xue, X. Yan, W. Yan, Q. Cheng, Y. Xie, *Nano Res.* 5 (2012) 521-530.
- [44] M.G. Walter, E.L. Warren, J.R. McKone, S.W. Boettcher, Q. Mi, E.A. Santori, N.S. Lewis, *Chem. Rev.* 110 (2010) 6446-6473.
- [45] M.F. Weber, M.J. Dignam, *J. Electrochem. Soc.* 131 (1984) 1258-1265.
- [46] Y. Gorlin, T.F. Jaramillo, *J. Am. Chem. Soc.* 132 (2010) 13612-13614.
- [47] N.H. Chou, P.N. Ross, A.T. Bell, T.D. Tilley, *ChemSusChem* 4 (2011) 1566-1569.
- [48] S.K. Singh, V.M. Dhavale, S. Kurungot, *ACS Appl. Mater. Interfaces* 7 (2015) 442-451.
- [49] H.A. Gasteiger, S.S. Kocha, B. Sompalli, F.T. Wagner, *Appl. Catal. B* 56 (2005) 9-35.
- [50] J. Suntivich, K.J. May, H.A. Gasteiger, J.B. Goodenough, Y. Shao-Horn, *Science* 334 (2011) 1383-1385.
- [51] K.-R. Wee, M.K. Brennaman, L. Alibabaei, B.H. Farnum, B. Sherman, A.M. Lapides, T.J. Meyer, *J. Am. Chem. Soc.* 136 (2014) 13514-13517.
- [52] M. Zhang, M. de Respinis, H. Frei, *Nat. Chem.* 6 (2014) 362-367.
- [53] H.-C. Chen, D.G.H. Hetterscheid, R.M. Williams, J.I. van der Vlugt, J.N.H. Reek, A.M. Brouwer, *Energy Environ. Sci.* 8 (2015) 975-982.
- [54] P. Comte, M.K. Nazeeruddin, F.P. Rotzinger, A.J. Frank, M. Grätzel, *J. Mol. Catal.* 52 (1989) 63-84.
- [55] P.K. Ghosh, B.S. Brunschwig, M. Chou, C. Creutz, N. Sutin, *J. Am. Chem. Soc.* 106 (1984) 4772-4783.
- [56] A. Lewandowska-Andralojc, D.E. Polyansky, R. Zong, R.P. Thummel, E. Fujita, *Phys. Chem. Chem. Phys.* 15 (2013) 14058-14068.
- [57] M.S. Baptista, J. Cadet, P.D. Mascio, A.A. Ghogare, A. Greer, M.R. Hamblin, C. Lorente, S.C. Nunez, M.S. Ribeiro, A.H. Thomas, M. Vignoni, T.M. Yoshimura, *Photochem. Photobiol.* 93 (2017) 912-919.
- [58] L. Francàs, C. Richmond, P. Garrido-Barros, N. Planas, S. Roeser, J. Benet-Buchholz, L. Escriche, X. Sala, A. Llobet, *Chem. Eur. J.* 22 (2016) 5261-5268.
- [59] I. Bazzan, A. Volpe, A. Dolbecq, M. Natali, A. Sartorel, P. Mialane, M. Bonchio, *Catal. Today* 290 (2017) 39-50.
- [60] A.L. Kaledin, Z. Huang, Y.V. Geletii, T. Lian, C.L. Hill, D.G. Musaev, *J. Phys. Chem. A* 114 (2010) 73-80.
- [61] H.S. White, W.G. Becker, A.J. Bard, *J. Phys. Chem.* 88 (1984) 1840-1846.
- [62] D. Rehm, A. Weller, *Bunsenges Ber. Phys. Chem.* 73 (1969) 834.
- [63] D. Rehm, A. Weller, *Isr. J. Chem.* 8 (1970) 259.
- [64] F. Bolletta, M. Maestri, L. Moggi, *J. Phys. Chem.* 77 (1973) 861-862.
- [65] A.J. Bard, M.A. Fox, *Acc. Chem. Res.* 28 (1995) 141-145.
- [66] For a quantitative analysis of the band energy levels of similar Co<sub>3</sub>O<sub>4</sub> NPs, see: H. Zhang, S. Pokhrel, Z. Ji, H. Meng, X. Wang, S. Lin, C.H. Chang, L. Li, R. Li, B. Sun, M. Wang, Y.-P. Liao, R. Liu, T. Xia, L. Mädler, A. E. Nel, *J. Am. Chem. Soc.* 136 (2014) 6406-6420.